Signal Processing 155 (2019) 96–107

Contents lists available at ScienceDirect

Signal Processing

journal homepage: www.elsevier.com/locate/sigpro

Aperiodic geometry design for DOA estimation of broadband sources using compressive sensing

Zeeshan Asghar Sayed*, Boon Poh Ng

Nanyang Technological University, 50 Nanyang Ave, 639798 Singapore

ARTICLE INFO

Article history:
Received 25 November 2017
Revised 23 July 2018
Accepted 18 September 2018
Available online 21 September 2018

Keywords:
Compressive sensing
Aperiodic geometry

ABSTRACT

Antenna arrays used in Compressive Sensing (CS) based algorithms are generated randomly to minimize mutual coherence. This scheme, although good for compressive sensing, suffers from practical limitations. Random sampling of antenna aperture is impractical. Rectangular arrays, although uniform, suffer from poor performance when used in CS algorithms. It is particularly ill suited to algorithms designed to estimate DOA of broadband sources, because of the introduction of grating lobes. Aperiodic arrays offer some advantages in the CS scenario. The aperiodic geometries based on Penrose and Danzer tiling are inherently sparse as they utilize a fewer number of sensors as compared to the regular geometries. Based on minimization of mutual coherence, this paper develops a novel optimization scheme, that can generate sparse array geometries offering improved performance for CS algorithms. This paper demonstrates that it is possible to design aperiodic arrays that perform much better than rectangular arrays by using a simple disturbance optimization scheme, that can be applied to other aperiodic geometries as well. A greedy MMV based compressive sensing algorithm, SOMP, is used to evaluate the performance of a number of geometries. Two geometries have been identified that perform better than all other geometries studied, including the random-sampling based geometries.

1. Introduction

Compressive sensing [4–7] has gained considerable attention in literature recently. It has been applied to many problems including image processing, image compression, radar signal processing, array signal processing, etc. The problem of array geometry pertaining to CS theory for broadband sources has not been studied very well.

The array geometry that is commonly used for direction of arrival estimation is Uniform Linear Array (ULA) or its 2-D counterpart, Rectangular Grid Array (RGA) [3]. The neighboring elements in the aforementioned array geometries, on each axis, are separated by a fixed distance, $\frac{\lambda}{2}$. λ being the wavelength of the carrier signal. The configuration works well if the sole purpose is to achieve compression in frequency domain. But if the design objective is to compress the number of array elements, then this configuration is not suitable. A random sampling of aperture is much more suitable [15].

Herman et al.[16] and Ender [17] studied application of compressive sensing to the radar problem and gave some initial results regarding the potential of using CS to address DOA estimation problem. Ender addresses several radar problems, including pulse compression, Inverse Synthetic Aperture Radar (ISAR) and radar DOA estimation. Both these papers, however, use a geometry that is achieved through random sampling of the aperture. Random sampling of aperture generates a measurement matrix that is well suited to use with CS algorithms, as it reduces the mutual coherence of the Basis vectors. Such a geometry is not practically feasible. The main reason is that there is no underlying geometry in a randomly sampled aperture. Usually, in a randomly sampled aperture, some of the elements would lie too close to each other which is not practically realizable.

The study of sparse array geometry is a rapidly developing topic. The MUSIC [20] algorithm is industry standard for use in DOA estimation problem. Ma et al. [21] developed a subspace augmentation technique based on Khatri-Rao product that effectively created “virtual sensors”, so that the DOA for more sources can be estimated than the number of sensors. Nested arrays have been utilized by Pal et al. [22] to increase the number of virtual sensors and estimate more sources than the number of sensors. In some of already developed techniques, during the formation of the covariance matrix for the MUSIC algorithm, the difference co-array is utilized instead of using the standard approach of calculating covariance matrix from multiple time-domain snapshots of data

* Corresponding author.
E-mail addresses: sayed1@e.ntu.edu.sg (Z. Asghar Sayed), ebpng@ntu.edu.sg (B.P. Ng).

https://doi.org/10.1016/j.sigpro.2018.09.026
0165-1684/

measurements. Qin et al. [23] have developed a generalized scheme to generate a geometry based on co-prime array concept. In this method two linear sub arrays are used to generate a difference co-array. This approach increases the effective number of degrees of freedom for the direction of arrival estimation. Two concepts of co-prime arrays are introduced, one is co-prime Array with Compressed Inter-element Spacing (CACIS) in which one of the array is compressed by an integer factor to reduce the inter-element spacing of the array. Another structure studied is the Co-prime Array with Displaced Sub-arrays (CADiS). This array structure indeed offer some advantages related to the degrees of freedom for creating covariance matrix, however, this technique is currently limited to linear arrays.

The use of aperiodic geometry can reduce the problem of random aperture sampling significantly and make the layout practically realizable. Fractal geometries [19,24] have effectively been used in the design of aperiodic arrays. These studies, however, utilize classical array processing framework and much of the results may not be applicable to compressive sensing scenario. In [13], Spence et al. introduce a design technique to generate antenna array layouts from aperiodic tiling. The technique uses a slight perturbation in inflation technique to generate aperiodic tiling. They have used Genetic Algorithm (GA) based optimization scheme to achieve low sidelobe levels and no grating lobes over wide bandwidths. This technique, however, is suitable for conventional array signal processing algorithms. Its scope is also different from what we intend to explore in this paper. Asghar et al. [1] studied aperiodic array geometry optimization for narrowband sources. The optimization scheme developed is limited to narrowband signals.

In this paper, we device an optimization technique, that generates antenna-array layout through a disturbance of initial conditions for aperiodic geometry. The choice of the aperiodic geometry has been made due to its inherent sparsity. We were also inspired by the discovery of "Quasicrystals" in materials found in nature [18]. The optimization method developed in this paper, however, is quite general in a sense that it can be applied to both broadband and narrowband cases, as well as to geometries other than the aperiodic geometries specifically studied here. Any array geometry that can be formed by linear transformation of a few initial points is a potential candidate for the optimization scheme developed. The linear transformations include translations, rotations, scalings, etc. The only design parameters for this optimization scheme are the positions of the initial sets of points. The motivation behind developing the optimization scheme is to firstly, build an array geometry than is sparse and secondly, it performs well for broadband source DOA estimation for a sparse recovery CS algorithms by minimization of the mutual coherence of the columns of the array manifold matrix.

The rest of the paper is organized as follows. In Section 2, we study different properties of the array manifold matrix (or the measurement matrix) relevant to the geometrical design. In Section 3, we discuss different aperiodic array geometries used for study in this paper. In Section 4, we develop an optimization technique to generate aperiodic array layout. Section 5 describes the simulation setup. The array geometries used in this paper and the performance results are discussed in Sections 6 and Section 7, respectively. Finally, in Section 8, we present conclusions.

Notations: The scalars are represented by small letters, a and capital letters, A. The vectors are represented by emboldened small letters, $\boldsymbol{a}$. Matrices are represented by capital bold letters, $\boldsymbol{A}$. $\|A\|_0$ represents the non-zero rows contained in the matrix, $\boldsymbol{A}$.

2. The array manifold matrix

Direction of arrival estimation system consisting of M sensors (array elements), for K broadband sources, with r time domain snapshots, can be described by the following frequency-domain mathematical equation:

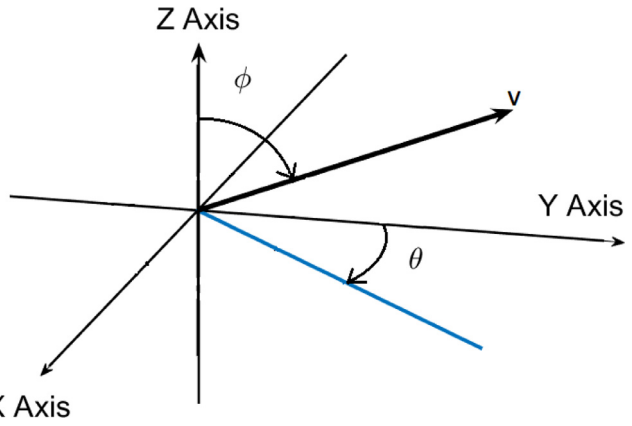

Fig. 1. The coordinate system. A vector $\boldsymbol{v}$ is pointing in directions θ and ϕ and has length $\|\boldsymbol{v}\|$.

$$\boldsymbol{Y}(f) = \boldsymbol{A}(f)\boldsymbol{X} + \boldsymbol{H}(f), \tag{1}$$

where,

$$\|\boldsymbol{X}\|_0 = K. \tag{2}$$

$\boldsymbol{Y}(f), \boldsymbol{H}(f) \in \mathbb{C}^{M\times r}$ represent sensor outputs converted to frequency-domain and additive noise matrix, respectively. $\boldsymbol{H}(f)$ contains the noise vectors, assumed to have complex Normal distribution, $\mathcal{CN}(0, \sigma^2\boldsymbol{I})$. $\boldsymbol{X}(f)$ is the vector containing signals originating from K sources and is K-sparse as indicated by (2). $\boldsymbol{A}(f) \in \mathbb{C}^{M\times N}$ is the frequency dependent *array manifold matrix*. It is formed by stacking N steering vectors, $\boldsymbol{a}(f, \theta, \phi)$, as the columns.

The coordinate system used is shown in Fig. 1. The steering vector, as a function of frequency, f and directions, θ and ϕ, is given by:

$$\boldsymbol{a}(f, \theta, \phi) = \frac{1}{\sqrt{M}}\left[e^{j\boldsymbol{\kappa}_{\theta,\phi}^T\boldsymbol{p}_1}, \ldots, e^{j\boldsymbol{\kappa}_{\theta,\phi}^T\boldsymbol{p}_M}\right]^T, \tag{3}$$

where, $f \in \mathbb{R}$, $\theta \in (0, 2\pi]$ and $\phi \in [0, \pi]$. $\boldsymbol{p}_i$ is the position vector for i^{th} sensor. $\boldsymbol{P}$ is a matrix containing all the positions vectors, $\boldsymbol{p}_i$'s, of M sensors. The wavenumber vector, $\boldsymbol{\kappa}_{\theta,\phi}$ is given by $\boldsymbol{\kappa}_{\theta,\phi} = \frac{2\pi f}{\nu}\boldsymbol{v}_{\theta_s}$. ν represents the speed of the carrier photons. $\boldsymbol{v}_{\theta,\phi}$ is the unit vector in the direction of source, defined as:

$$\boldsymbol{v}_{\theta,\phi} := (\cos\theta\sin\phi, \sin\theta\sin\phi, \cos\phi). \tag{4}$$

N represents the number of discrete directions, in which the DOA space is quantized. N is factored, in case of, two DOA parameters as following:

$$N = N_\theta N_\phi. \tag{5}$$

Here, N_θ represents the number of horizontal (azimuth) directions, while, N_ϕ represents the number of vertical (polar angle) directions.

For the noiseless, single-snapshot system, $\boldsymbol{y} = \boldsymbol{\Phi}\boldsymbol{\Psi}\boldsymbol{x}$, for complete recovery of $\boldsymbol{x}$, given $M \ll N$, an important property, that the matrix $\boldsymbol{A}(f)$ should observe, is the Restricted Isometry Property [8]. For each integer $K = 1, 2, \ldots,$ define the isometry constant δ_K of a matrix $\boldsymbol{A}(f)$ as the smallest number such that

$$(1-\delta_K)\|\boldsymbol{x}\|_2^2 \le \|\boldsymbol{A}(f)\boldsymbol{x}\|_2^2 \le (1+\delta_K)\|\boldsymbol{x}\|_2^2, \tag{6}$$

holds for all sparse vectors $\boldsymbol{x}$. Matrix $\boldsymbol{A}(f)$ obeys Restricted Isometry Property (RIP) of order z, if δ_K is not too close to 1. The RIP condition ensures that K-sparse signals should not reside in the null space of $\boldsymbol{A}(f)$, otherwise, these signals would not be recoverable.

One of the few matrices that observe this property is the Fourier matrix [8,9]. $\boldsymbol{A}(f)$, in fact is a Fourier matrix, containing complex Fourier basis as its columns.

Another significant parameter is the mutual coherence, μ, which indicates the level of sparsity that can be recovered with very high probability. μ is defined by the following equation:

$$\mu(\boldsymbol{\Phi}, \boldsymbol{\Psi}) = \sqrt{N} \max_{1 \le k, j \le N} |\langle \boldsymbol{\Phi}_k, \boldsymbol{\Psi}_j \rangle|. \tag{7}$$

If the number of measurements, M, for K-sparse vector obeys the following inequality

$$M \geq C\mu(\boldsymbol{\Phi}, \boldsymbol{\Psi})^2 K \log(N), \tag{8}$$

for some positive constant, C, then the solution to this problem is exact with "overwhelming probability" [8]. Here, the Matrix $\boldsymbol{A}(f) = \boldsymbol{\Phi}\boldsymbol{\Psi}$. For the case of DOA estimation $\boldsymbol{\Psi}$ is the identity matrix as the sparsity is in the spacial domain. These properties relate to the *array manifold matrix* or *the measurement matrix*, which is common to all systems, whether utilizing single snapshot or multiple snapshots.

For the case of multiple snapshots (MMV) [12], we use a CS based greedy sparse recovery algorithm called Simultaneous Orthogonal Matching Pursuit (SOMP) [10,11] for our simulations to study different array geometries.

The problem of the direction of arrival estimation is actually estimation of a few parameters; azimuth, θ in the case of 2D Cartesian coordinates or linear array, azimuth and the polar angle (θ, ϕ) in the case of 3D Cartesian coordinates and planar array.

The geometry is dictated by the arrangement of the sensor array elements. If the array elements form a curve only one parameter can be estimated. In case the sensor elements span a 2D plane, however irregular, both the parameters (azimuth and polar angle) can be estimated, at least theoretically.

In this paper, we will focus on the planar array geometry, and study a specific class of geometries based on aperiodic tiling. The main reason for choosing this geometry is that it is inherently sparse, as would become apparent in the coming sections.

3. Aperiodic tiling based array geometry

A 2-D aperiodic tiling consists of a collection of tiles that divide the 2-D plane in such a way that it lacks horizontal or vertical translational symmetry. A periodic tiling, however, contains both horizontal and vertical translational symmetry. A set of shapes, called prototiles, are used to populate the whole 2-D plane. These prototiles vary in numbers. To populate a 2-D plane periodically with a square tile would require just one prototile. On the other hand, populating a 2-D plane randomly would require an infinite number of prototiles. However, there are ways in which one could populate the whole 2-D plane aperiodically using just a few prototiles. Penrose [2] discovered a two-prototile set (called kite and dart) that could fill up a 2-D plane aperiodically, if the tiles are placed together with certain predefined rules. One way to define the rules is to place colored lines on each tile. A tile could only be be placed in a certain location if the lines are contiguous. This would ensure that there are no gaps left while the tiling process is being applied. But there is a problem with this scheme as we can arrive at a point where no further tiles could be added due to the matching rules.

Another more robust iterative method called "inflation" is also used for tiling the plane aperiodically. A tile is first enlarged and is subsequently subdivided into it's constituent tiles. This process is repeated until the plane is filled completely.

Later in this section, we discuss a particular set of geometries based on aperiodic tiling. Aperiodic tiling based array geometries have a lot of promise as these geometries are inherently sparse and require very few sensors as compared to the uniform geometry. Additionally, aperiodicity of the array geometry is a desirable trait, as it can be exploited to make the rows of the measurement matrix as much orthogonal as possible, resulting in a small mutual coherence.

The motivation here is to identify sets of geometries that are better suited to compressed sensing based direction of arrival estimation algorithms. Next we describe two aperiodic tiling schemes and array geometries based on these schemes. We have used Penrose and Danzer aperiodic tiling schemes as base for generation of the aperiodic array geometries for CS based DOA estimation of broadband sources.

3.1. Penrose tiling

Penrose tiling [2] consists of two base tiles *AL* and *AS*, as shown in Fig. 2. These two tiles can be used to fill any 2-D plane in an aperiodic fashion. There are two methods to do that. The first method is rule based. It starts from a single tile and based on edge matching rules building tiles around the tile resulting in an ever growing structure. This method can run into problems when the tiles can no more be placed seamlessly. The other method is called "inflation". In this method each tile is scaled up by a factor and is then sub-divided into the base tiles AL and AS. This process is repeated until the desired plane is completely filled. Fig. 3 shows the inflation process after the first iteration.

3.2. Danzer tiling

Danzer tiling [14] consists of three base tiles type-1, type-2 and type-3. These three tiles can be used to fill any 2-D plane in an aperiodic fashion. Fig. 4 shows the tiles after first iteration of the inflation process.

Within each base tile we select a single point that corresponds to the position of the sensor and after performing the inflation process for several iterations we arrive at the desired geometry by replacing each tile by the corresponding sensor. The aperture is usually fixed and the only variable is the number of sensors. Fig. 5 shows the sensor placement after three iterations of the inflation process. The sensor is placed at the vertices of each base tile and the redundant sensors are removed.

4. Optimization scheme

The measurement matrix depends on three parameters, n, m and l. n is the steering direction, m is the index of the array element position vector and l is the frequency-bin. Note that in the narrowband case, the parameter l would be absent as there are only a very narrow band of frequencies which can be approximated as a single frequency. In that case, we can drop l from the subsequent equations. Each element of the matrix, $\boldsymbol{A}(f)$, can be written as:

$$\boldsymbol{A}_l(m, n) = e^{j\kappa_l \boldsymbol{p}_m^T \boldsymbol{r}_n}. \tag{9}$$

Where, $l \in \{1, \ldots, L\}, m \in \{1, \ldots, M\}, n \in \{1, \ldots, N\}$. κ_l is the magnitude of wavenumber vector for frequency bin l. $\boldsymbol{p}_m$ is the position vector for sensor m, while, $\boldsymbol{r}_n$ is the unit vector for direction index, n. L represents the number of frequency bins, M is the number of array sensors, while N is the number of directions, given by (5).

We define a matrix, $\boldsymbol{B}_l := \boldsymbol{A}_l \boldsymbol{A}_l^H$. The matrix $\boldsymbol{B}_l$ gives the dot product of the rows of the matrix $\boldsymbol{A}_l$ and for frequency index, l and it is given by:

$$\boldsymbol{B}_l(u, v) = \sum_{\xi=1}^{N} e^{j\kappa_l (\boldsymbol{p}_u^T \boldsymbol{r}_\xi - \boldsymbol{p}_v^T \boldsymbol{r}_\xi)}. \tag{10}$$

(a) Tile AL (b) Tile AS

Fig. 2. Basic Penrose Tiles.

(a) Tile AL (b) Tile AS

Fig. 3. Level I Penrose Tiles.

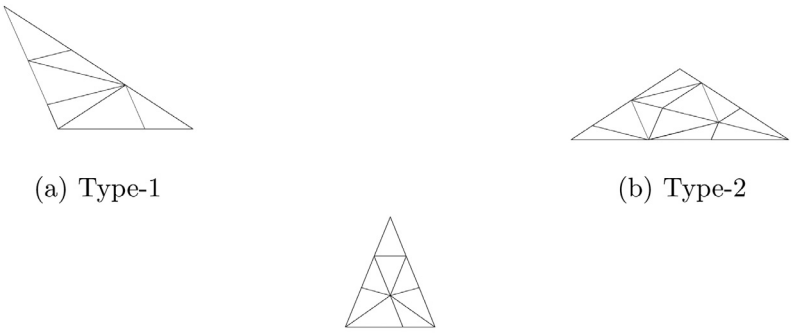

(a) Type-1 (b) Type-2

(c) Type-3

Fig. 4. Level I Danzer Tiles.

(a) Level-III Danzer aperiodic tiling (b) Sensors array antenna formed by placing sensors at the indices of each triangle (tile)

Fig. 5. Illustration of the formation of aperiodic array geometry from the corresponding tiling.

Note that we have L such matrices, one matrix each for every value of frequency index, l. For narrowband case, just one matrix, $\boldsymbol{B}$ would suffice. We define a matrix $\boldsymbol{B} \in \mathbb{C}^{(ML)\times(ML)}$,

$$\boldsymbol{B} = \begin{bmatrix} \boldsymbol{B}_1 & \mathbf{0} & \mathbf{0} & \mathbf{0} & \mathbf{0} \\ \mathbf{0} & \ddots & \mathbf{0} & \mathbf{0} & \mathbf{0} \\ \mathbf{0} & \mathbf{0} & \boldsymbol{B}_l & \mathbf{0} & \mathbf{0} \\ \mathbf{0} & \mathbf{0} & \mathbf{0} & \ddots & \mathbf{0} \\ \mathbf{0} & \mathbf{0} & \mathbf{0} & \mathbf{0} & \boldsymbol{B}_L \end{bmatrix}. \tag{11}$$

Where, $\boldsymbol{0} := 0^{M\times M}$.

Each matrix $\boldsymbol{B}_l$ is the autocorrelation matrix of $\boldsymbol{A}_l$, according to (10). The later matrix being the array manifold matrix for frequency bin l. The matrix $\boldsymbol{A}_l(m, n)$ is dependent on two variables: m, n. The direction of the sources, n, is fixed. The degree of freedom for this matrix comes from the position of the sensors, which is controlled by variable m, as $\boldsymbol{p}_m$ is the location of m^{th} sensor. Given a matrix,$\boldsymbol{A}_l$, with N columns, our aim is control the position of the sensors in such a manner that the rows of the matrix $\boldsymbol{A}_l$ become orthogonal. This would lead to the matrix $\boldsymbol{A}_l$ having a smaller mutual coherence, μ (7), thus becoming more suitable for application of CS algorithms. If the rows of matrix $\boldsymbol{A}_l$ are orthogonal, the matrix $\boldsymbol{B}_l$ would become and identity matrix.

Our objective is to find sensor locations that would result in matrix $\boldsymbol{B}_l$ becoming an identity matrix. In case of aperiodic tiling based geometry, as explained earlier, we choose initial points within base tiles such that the matrix $\boldsymbol{B}_l$ is as close to the identity matrix as possible. Since matrix $\boldsymbol{B}$ is constructed from several matrices $\boldsymbol{B}_l$, our objective now becomes to find a matrix $\boldsymbol{B}$ that is and identity matrix.

To meet our objectives, we pose the following optimization problem:

$$\underset{\boldsymbol{p}}{minimize} \quad \|\boldsymbol{B} - \lambda \boldsymbol{I}_{ML}\|_2 \tag{12}$$

$$subject\ to \quad \boldsymbol{M}_u \boldsymbol{p} + \boldsymbol{C}_u \leq 0.$$

(a) Tile AL (b) Tile AS

Fig. 6. Optimization constraints depicted by boundary lines for Penrose tiles.

(a) Level IV Penrose Tile AL (Danzer Geometry 1). (b) Level II Danzer Tile 1 (Danzer Geometry 2).

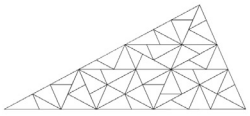

(c) Level II Danzer Tile 2 (Penrose Geometry 1).

Fig. 7. Different types of Penrose geometries used for simulations.

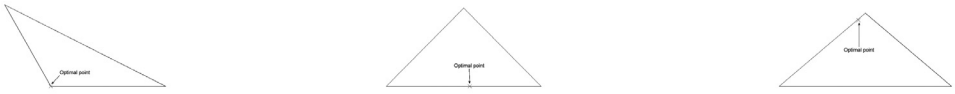

(a) Tile 1 (b) Tile 2 (c) Tile 3

Fig. 8. Optimal points for "Danzer Geometry 1" a) Danzer Tile 1, b) Danzer Tile 2, c) Danzer Tile 3.

(a) Tile 1 (b) Tile 2 (c) Tile 3

Fig. 9. Optimal points for "Danzer Geometry 2" geometry a) Danzer Tile 1, b) Danzer Tile 2, c) Danzer Tile 3.

(a) Tile 1 (b) Tile 2

Fig. 10. Optimal points for "Penrose Geometry 1" a) Penrose Tile AL, b) Penrose Tile AS.

Here, $\boldsymbol{M}_u$ and $\boldsymbol{C}_u$ contains slopes and y-intercepts, respectively, of the base triangle boundaries. The inequality would constrain the initial points to lie on the boundary or inside the base triangles. The matrices $\boldsymbol{M}_u$ and $\boldsymbol{C}_u$ are described in a later section. λ is an optimization constant.

In its current form, this problem does not seem to be solvable. What we do next would pave the way for finding a solution to this problem.

We have seen in Section 3.2, that the aperiodic array is manufactured by starting with just three points. Thus each element of the array $\boldsymbol{p}_u$, can be written as $\boldsymbol{T}_u\boldsymbol{p}$, where, $\boldsymbol{p}$ contains the initial two or three points, depending on the base geometry. The matrix, $\boldsymbol{T}_u$, is the transformation matrix obtained using the inflation process. It contains all the necessary transformations to transform the initial points to form a complete geometry. Making this substitution, (10) becomes

$$\boldsymbol{B}_l(u,v) = \sum_{\xi=1}^{N} e^{jk_l((\boldsymbol{T}_u\boldsymbol{p})^T\boldsymbol{r}_\xi - (\boldsymbol{T}_v\boldsymbol{p})^T\boldsymbol{r}_\xi)}. \tag{13}$$

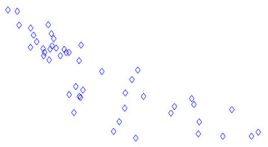

(a) 48-element random array

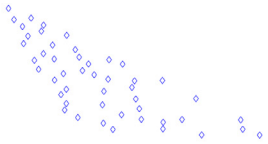

(b) 48-element constrained random array

(c) 60-element triangular array (rectangular grid sampling)

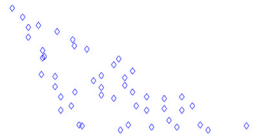

(d) 48-element Danzer array

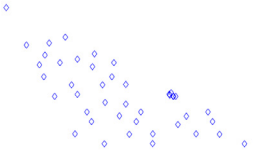

(e) 48-element optimized aperiodic array

Fig. 11. Danzer Tile 1 aperture.

(a) 87-element random array

(b) 87-element constrained random array

(c) 111-element triangular array (rectangular grid sampling)

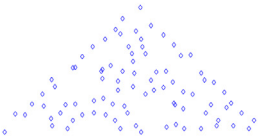

(d) 87-element Danzer array

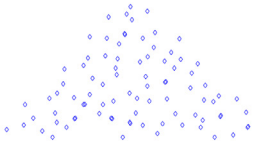

(e) 87-element optimized aperiodic array

Fig. 12. Danzer Tile 2 aperture.

Discarding the summation notation, and expanding the expression,

$$\boldsymbol{B}_l(u,v) = e^{j\kappa_l((\boldsymbol{T}_u\boldsymbol{p})^T\boldsymbol{r}_1-(\boldsymbol{T}_v\boldsymbol{p})^T\boldsymbol{r}_1)} + \ldots + e^{j\kappa_l((\boldsymbol{T}_u\boldsymbol{p})^T\boldsymbol{r}_N-(\boldsymbol{T}_v\boldsymbol{p})^T\boldsymbol{r}_N)}. \tag{14}$$

Since $\left[(\boldsymbol{T}_u\boldsymbol{p})^T-(\boldsymbol{T}_v\boldsymbol{p})^T\right]\boldsymbol{r}_\xi$ is a scalar, we can transpose it to get the following expression:

$$\left[(\boldsymbol{T}_u\boldsymbol{p})^T-(\boldsymbol{T}_v\boldsymbol{p})^T\right]\boldsymbol{r}_\xi = \boldsymbol{r}_\xi^T\left[(\boldsymbol{T}_u\boldsymbol{p})^T-(\boldsymbol{T}_v\boldsymbol{p})^T\right]^T \tag{15}$$

$$= \boldsymbol{r}_\xi^T[\boldsymbol{T}_u\boldsymbol{p}-\boldsymbol{T}_v\boldsymbol{p}] \tag{16}$$

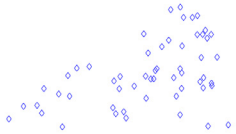

(a) 45-element random array

(b) 45-element constrained random array

(c) 48-element uniform sampling array

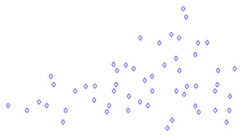

(d) 45-element Penrose array

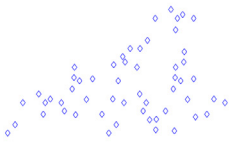

(e) 45-element optimized aperiodic array

Fig. 13. Penrose Tile AL aperture.

Table 1
Parameters used for the optimization problem in (26).

Parameter	Danzer Geometry 1	Danzer Geometry 2	Penrose Geometry 1
Number of sensors	48	87	45
Sampling frequency (f_s)	1	1	1
Centre frequency (f_c)	0.3	0.3	0.3
Bandwidth	0.24	0.24	0.24

Table 2
Parameters for simulation.

Parameter	Danzer Geometry 1	Danzer Geometry 2	Penrose Geometry 1
Number of sensors	48	87	45
Sampling frequency (f_s)	1	1	1
Centre frequency (f_c)	0.3	0.3	0.3
Bandwidth	0.24	0.24	0.24
Horizontal aperture	$12\lambda_{\min}$	$20\lambda_{\min}$	$20\lambda_{\min}$
Sources azimuth (degrees)	60, 94, 144	78, 94, 114	78, 94, 114
Sources elevation (degrees)	0	0	0
Frequency bins	256	256	256
Snapshots	2	2	2
Detection window (degrees)	4	3	3

$$= \boldsymbol{r}_{\xi}^{T}[\boldsymbol{T}_u - \boldsymbol{T}_v]\boldsymbol{p} \tag{17}$$

When $u = v$, the argument of exponentials all go to zero, and we have

$$\sum_{\xi=1}^{N} e^{j\kappa_0 0} = \chi. \tag{18}$$

This condition can be satisfied if we multiply each column of $\boldsymbol{A}_l$ by $\frac{\chi}{N}$.

For the diagonal entries, when $u \neq v$, the orthogonality condition is satisfied if,

$$e^{j\kappa_l(\boldsymbol{r}_1^T[\boldsymbol{T}_u-\boldsymbol{T}_v]\boldsymbol{p})} + \ldots + e^{j\kappa_l(\boldsymbol{r}_N^T[\boldsymbol{T}_u-\boldsymbol{T}_v]\boldsymbol{p})} = 0. \tag{19}$$

We can choose the arguments of exponentials (on a unit circle) in such a way that their sum becomes equal to zero, that is,

$$e^{j\epsilon_1} + e^{j\epsilon_2} + \ldots + e^{j\epsilon_N} = 0. \tag{20}$$

This gives rise to the following set of equations, for each (u, v) pair:

$$\begin{aligned} \boldsymbol{r}_1^T[\boldsymbol{T}_u - \boldsymbol{T}_v]\boldsymbol{p} &= \epsilon_{1,l} \\ &\vdots \\ \boldsymbol{r}_N^T[\boldsymbol{T}_u - \boldsymbol{T}_v]\boldsymbol{p} &= \epsilon_{N,l}. \end{aligned} \tag{21}$$

Here, $\epsilon_{i,l} := \frac{\epsilon_i}{\kappa_l}$. And $\boldsymbol{\epsilon}_l := [\epsilon_{1,\,l} \cdots \epsilon_{N,\,l}]^T$. The parameter, ϵ_i represents phase. We can chose $\epsilon_i = \frac{i}{2\pi N}$, to satisfy (20).

We define, $\hat{\boldsymbol{T}}_{u,v} := \boldsymbol{R}^T(\boldsymbol{T}_u - \boldsymbol{T}_v)$. Where, $\boldsymbol{R} := [\boldsymbol{r}_1 \cdots \boldsymbol{r}_N]$. All the combined equations for indices $u \in \{1, .M\}$, $v \in \{1, \ldots, M\}$ and $l \in \{1, ., L\}$ could be written into one huge matrix equation,

$$\boldsymbol{T}\boldsymbol{p} = \boldsymbol{\epsilon}. \tag{22}$$

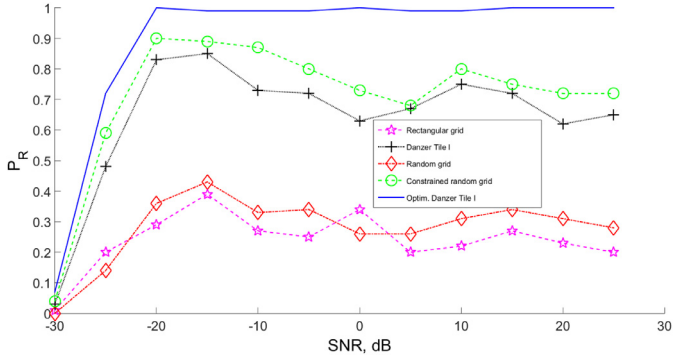

Fig. 14. SNR vs the probability of resolution (P_R) for Danzer Tile 1 aperture.

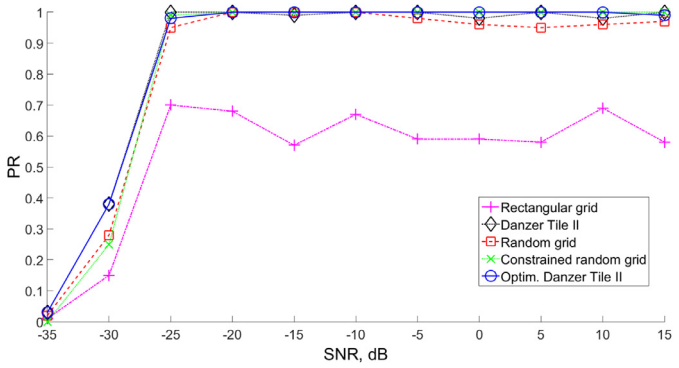

Fig. 15. SNR vs the probability of resolution (P_R) for Danzer Tile 2 aperture.

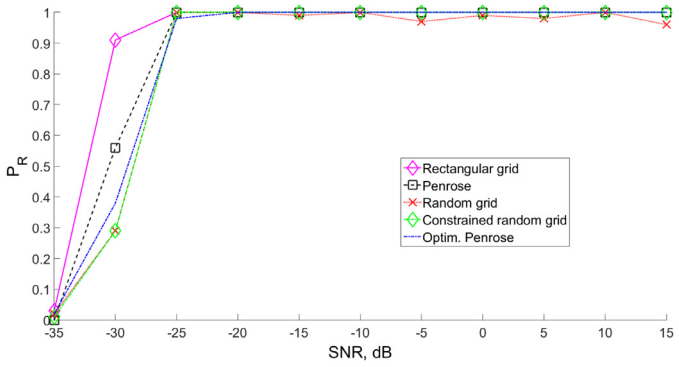

Fig. 16. SNR vs the probability of resolution (P_R) for Penrose Tile AL aperture.

Here,

$$\boldsymbol{T} := \begin{bmatrix} \hat{\boldsymbol{T}}_{1,2} \\ . \\ . \\ \hat{\boldsymbol{T}}_{1,M-1} \\ \hat{\boldsymbol{T}}_{2,1} \\ . \\ . \\ . \\ \hat{\boldsymbol{T}}_{M,M-1} \end{bmatrix}, \tag{23}$$

and $\boldsymbol{\epsilon} := \left[\boldsymbol{\epsilon}_1^T \cdots \boldsymbol{\epsilon}_L^T\right]^T$. We define,

$$\boldsymbol{\Upsilon} := \begin{bmatrix} \boldsymbol{T} \\ . \\ . \\ \boldsymbol{T} \end{bmatrix}, \tag{24}$$

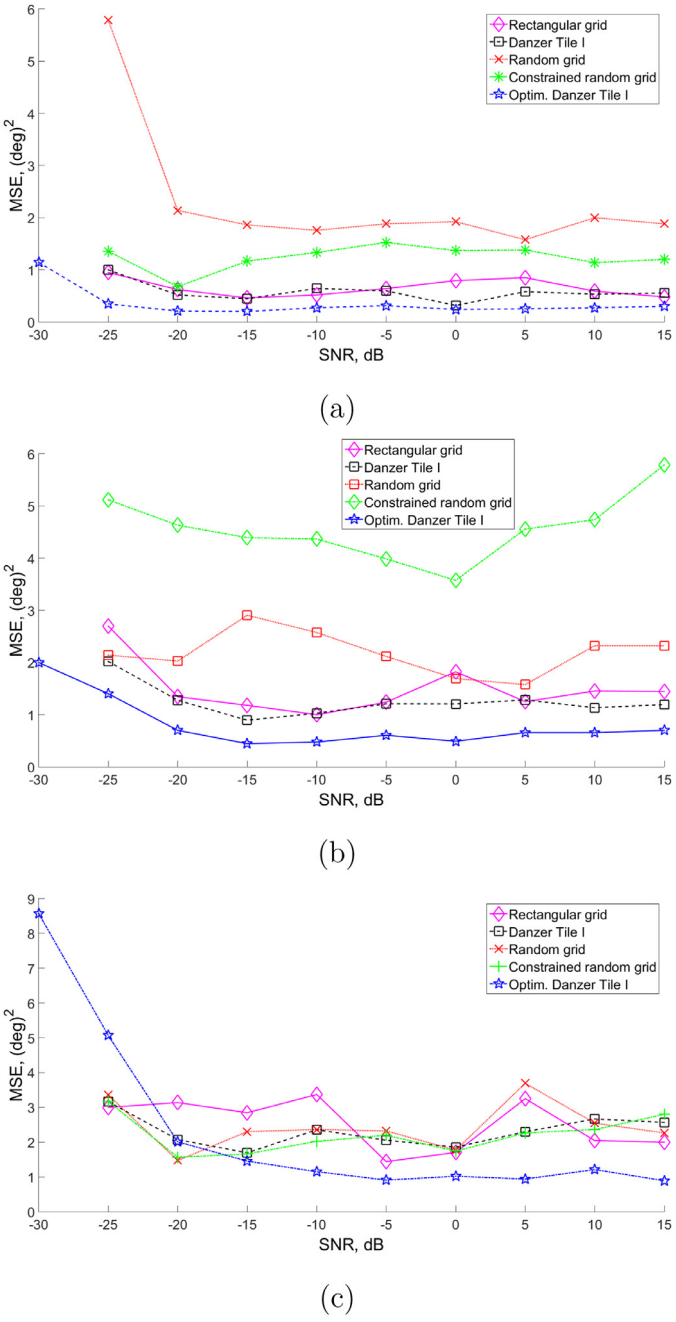

Fig. 17. MSE plot for geometries based on Danzer Tile 1 aperture a) Source 1 at 60 degrees azimuth, b) Source 2 at 94 degrees azimuth, c) Source 3 at 144 degrees azimuth. Note that the vertical axis is not constant for the sub-figures.

and

$$\boldsymbol{E} = [\boldsymbol{\epsilon}^T, \boldsymbol{\epsilon}^T \ldots \boldsymbol{\epsilon}^T]^T. \tag{25}$$

This gives rise to the following optimization problem:

$$\begin{aligned} &\underset{\boldsymbol{p}}{minimize} \quad \|\boldsymbol{\Upsilon}\boldsymbol{p} - \boldsymbol{E}\|_2 \\ &subject\ to \quad \boldsymbol{M}_u\boldsymbol{p} + \boldsymbol{C}_u \leq 0. \end{aligned} \tag{26}$$

This is a least squares problem with linear inequality constraints and is a convex problem, if the constraints are well defined.

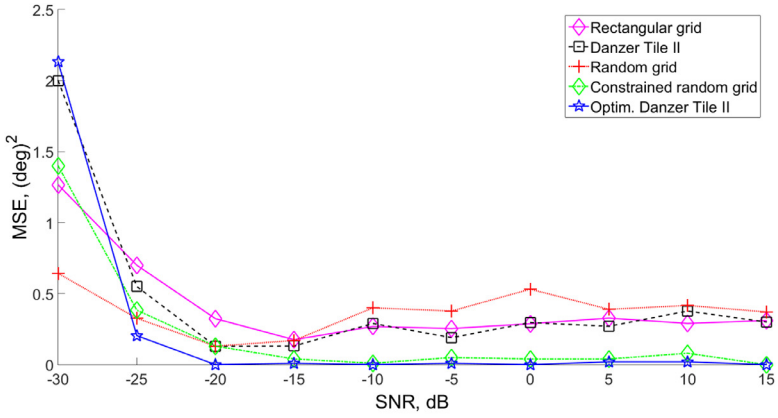

(a)

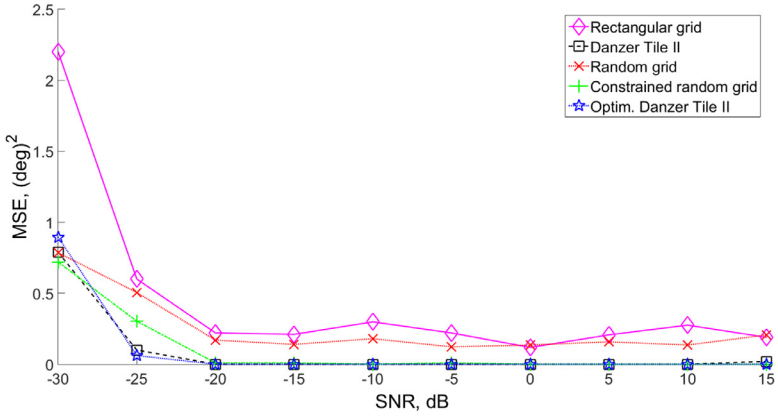

(b)

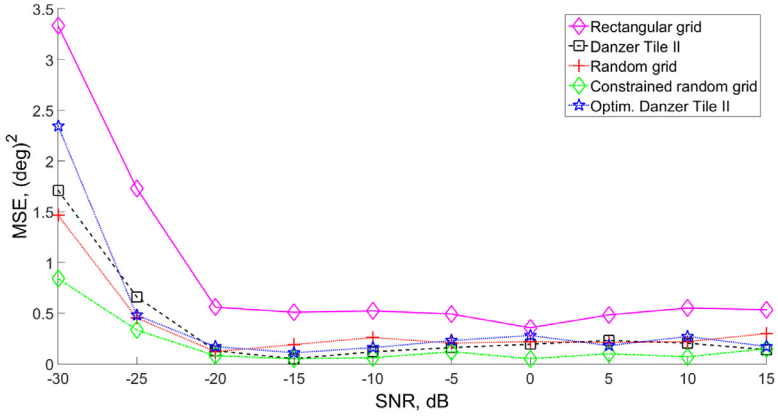

(c)

Fig. 18. MSE plot for geometries based on Danzer Tile 2 aperture a) Source 1 at 78 degrees azimuth, b) Source 2 at 94 degrees azimuth, c) Source 3 at 114 degrees azimuth. Note that the vertical axis is not constant for the sub-figures.

4.1. Boundary constraints for the optimization problem

The boundary constraints are given by the following inequality:

$$\boldsymbol{M}_u \boldsymbol{p} + \boldsymbol{C}_u \leq 0. \tag{27}$$

This inequality ensures that the solution lies inside or on the triangle boundaries. Matrix $\boldsymbol{M}_u$ is a 3×2 matrix. The first column of this matrix contains the slopes of the three edges of the triangles. The second column contains a value of 1 or -1 depending on whether we want to include points above or below this line.

Here, $\boldsymbol{M}_u = \begin{bmatrix} -d & 1 \end{bmatrix}$, when the interior of the triangle lies below the line, or $\boldsymbol{M}_u = \begin{bmatrix} d & -1 \end{bmatrix}$, when the interior of the triangle lies above the line defined by (d, c). $\boldsymbol{p}_u$ is a 2-vector, given by $\boldsymbol{p}_u = \begin{bmatrix} x & y \end{bmatrix}^T$. Similarly, $\boldsymbol{C}_u(k) = -c$, when the interior of the k^{th} triangle lies below the line and $\boldsymbol{C}_u(k) = c$, when it lies above.

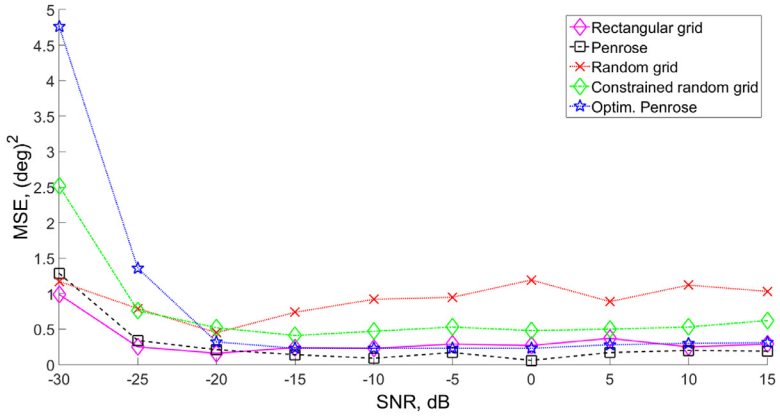

(a)

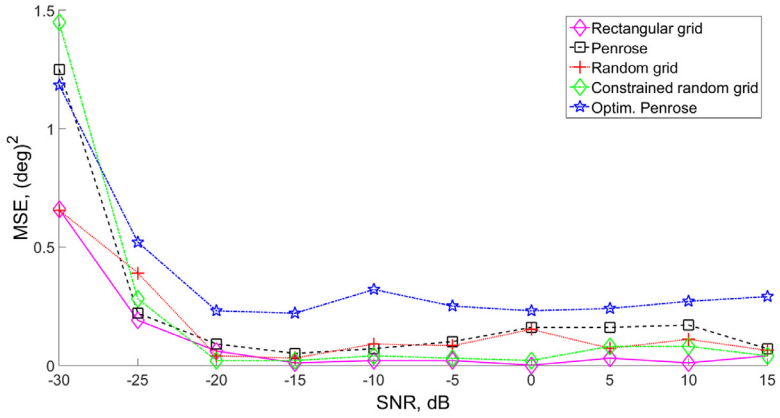

(b)

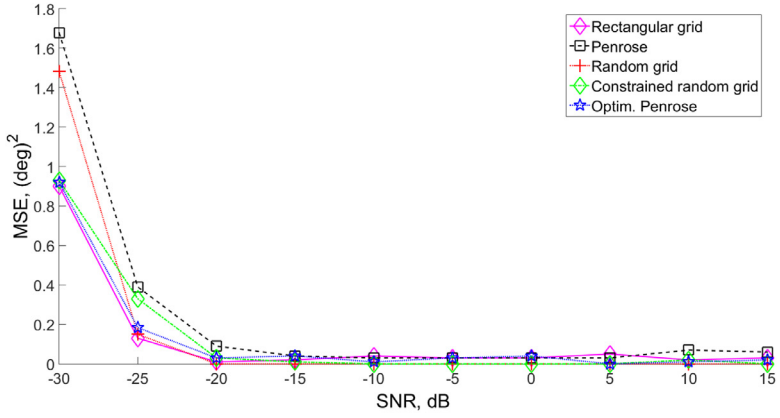

(c)

Fig. 19. MSE plot for geometries based on Penrose Tile AL aperture a) Source 1 at 78 degrees azimuth, b) Source 2 at 94 degrees azimuth, c) Source 3 at 114 degrees azimuth. Note that the vertical axis is not constant for the sub-figures.

Fig. 6 shows the boundary conditions for the two Penrose tiles. Similar Boundary conditions can be defined for Danzer tiles as well.

5. Simulation setup

The constrained least squares optimization (26) was performed for the following set of geometries:

i. Tile-1 Danzer Geometry at second iteration of inflation process, shown in Fig. 7 a (Henceforth referred to as "Danzer Geometry 1"). For all kinds of aperture sampling (including rectangular, random, etc.), the aperture for this geometry is the same, i.e., Tile-1 of Danzer tiling.
ii. Tile-2 Danzer Geometry at second iteration of inflation process, shown in Fig. 7 b (Henceforth referred to as "Danzer Geometry 2"). For all kinds of aperture sampling (including rectangular,

random, etc.), the aperture for this geometry is the same, i.e., Tile-2 of Danzer tiling.

iii. Tile-AL Penrose Geometry at fourth iteration of inflation process, shown in Fig. 7 c (Henceforth referred to as "Penrose Geometry 1"). For all kinds of aperture sampling (including rectangular, random, etc.), the aperture for this geometry is the same, i.e., Tile-AL of Danzer tiling.

The reason for choosing such an unconventional aperture is that our study relates to aperture sampling rather than the antenna aperture itself. Although antenna aperture does have some bearing on the output of the algorithm but we are more interested in the sampling of the aperture in this study. For this reason we have kept things simple by choosing the aperture as the base triangle for the respective geometry.

After solving the optimization problem (26) for all three geometries for the parameters given in Table 1, we get three optimal points for "Danzer Geometry 1" as shown in Fig. 8. All the three points lie on the boundary of the triangles. The result of optimization problem (26) for "Danzer Geometry 2" is shown in Fig. 9. In this case, the optimal points are close to the boundary but not located on the boundary itself. The result of optimization problem for "Penrose Geometry 1" is shown in Fig. 10. Here one point is located on the boundary (Tile AL) while the other point is away from the boundary (Tile AS).

6. Resultant geometries

After finding the optimal points, we can form the optimum sensor configuration for each case. To evaluate the performance of the optimized geometries, we need other configurations for comparison. We have used the following configurations:

i. **Random:** The random geometry is formed by generating random samples using a uniform distribution, within the aperture. The random sampling is very useful as it produces a measurement matrix having near orthogonal columns and very small mutual coherence.
ii. **Constrained random:** Since random geometry is not practical, as it would almost always contain samples too close to each other, the minimum spacing between two neighboring elements was constrained to $\frac{lambda}{3}$. This way the pseudo-randomness of the sampling is preserved but having the advantage of being practically implementable.
iii. **Uniformly sampled:** This form of sampling is the 2-D equivalent of Uniform Linear Array (ULA) but with the aperture constrained to a triangle instead of a square or a rectangle.
iv. **Base geometry:** This sampling is generated by taking arbitrary point, (0.5, 0.5), inside each base triangle and then generating the complete geometry using the transformation matrix.
v. **Optimized:** The optimal points are found using (26) and using these points the complete geometry is generated by using the inflation transformation matrix.

Fig. 11 shows different geometries generated using the "Danzer Geometry 1" aperture. The aperture for each geometry is the same (i.e Danzer Tile 1 (Fig. 7a)) for all the array configurations. The Horizontal distance between elements in uniformly sampled configuration is $d = \frac{\lambda_{\min}}{2}$. Where $\lambda_{\min} = \frac{c}{f_{\max}}$ and $f_{\max} = f_c + BW/2$. f_c being the center frequency and BW is the bandwidth of the broadband signal. As a result of optimization , the element spacing for the optimal geometry has reduced as compared to Danzer array (Fig. 11 d).

Fig. 12 shows different geometries generated using the "Danzer Geometry 2" aperture. The aperture for each geometry is the same i.e Danzer Tile 2 (Fig. 7b). The Horizontal distance between elements in uniformly sampled configuration is $d = \frac{\lambda_{\min}}{2}$.

Fig. 13 shows different geometries generated using the "Penrose Geometry 1" aperture. The aperture for each geometry is the same, i.e, Penrose Tile AL (Fig. 7c). The Horizontal distance between elements in uniformly sampled configuration is $d = \frac{\lambda_{\min}}{2}$.

7. Performance results

In this section, the performance of different geometries, introduced in the previous section, is analyzed. The performance of each geometry is analyzed at different SNR values, ranging from really poor (-35db) to good SNR (25db). Since we are dealing with compressive sensing scenario, the time domain snapshots (represented by r) are kept at the minimum ($r = 2$).

Table 2 lists the parameters used for 200 Montecarlo simulations that were performed to evaluate the performance of the SOMP algorithm for all the geometries discussed in Section (6).

The term probability of resolution (P_R) is defined for resolution of two sources in [3]. We have used the same definition when finding two sources. When we have more than two sources then the term probability of resolution is extended in the following manner. Suppose M sources are located at u_1, u_2, $\cdots$, u_M. We define the boundary between the adjacent source pairs $(u1, u2)$, $(u2, u3), \cdots,$ (u_{M-1}, u_M) as $\hat{u}_1, \cdots, \hat{u}_{M-1}$, where $\hat{u}_m = \frac{u_m - u_{m-1}}{2}$. The minimum bound for the first source is $\hat{u}_0 = u_1 - \delta$, while the maximum bound for the last source is $\hat{u}_0 = u_M + \delta$. δ is a small number. It quantizes the DOA space and should be chosen based on the aperture of the array. A smaller δ for a larger aperture and vice versa. In our simulations we have used values of δ as given in 2. The sources are considered resolved if all the M peaks lie within the boundaries defined.

The mean squared error for each source is evaluated over ξ simulations using the following equation:

$$MSE = \frac{1}{\xi}\sum_{i=1}^{\xi}(\theta - \hat{\theta})^2. \tag{28}$$

In the case of "Danzer Geometry 1", Fig. 14 shows the performance of the five different array configurations discussed in Section 6. The performance of the SOMP algorithm for the optimized geometry is much better as compared to the other geometries for the simulation parameters given in Table 2. Provided that the uniform sampling geometry has significantly more sensors than the other configurations, its performance is still the worse among all the geometries studied.

Fig. 15 shows the performance of different array configurations discussed in Section 6 based on "Danzer Geometry 2". Apart from the uniform grid geometry, the performance of other geometries is very similar. Optimal geometry has a marginal performance advantage over other geometries used for this simulation.

Fig. 16 shows the performance of different array configurations based on "Penrose Geometry 1" aperture. The performance based on simulation parameters given in Table 2, is better for the uniform sampling configuration, in comparison with other sampling paradigms.

In this case the optimum configuration did not offer any advantage over the rest of the geometries. Which would indicate that this geometry is not well suited to the optimization problem being studied in this paper. Please note that in case of random sampling based geometry the increase in SNR either doesn't improve the performance but in some cases has an adverse effect on the performance. The reason is that for unconstrained random geometry there is a very high probability that two or more sensors would lie very close to each other at one or multiple locations. The effect is that the rows associated with these sensors in the array manifold matrix would be almost identical, thus resulting in a covari-

ance matrix that would be rank deficient regardless of the number of snapshots or an increase in SNR.

The performance, according to the MSE criterion, has a similar pattern. For "Danzer Geometry 1", Fig. 17 shows the MSE vs SNR plots for the three sources given in Table 2, i.e., 60, 94, 144 degrees azimuth, with elevation kept at zero degree. For all the three sources, the MSE results of the optimal configuration are better than the rest of the configurations. Fig. 18 shows the MSE vs SNR plots for "Danzer Geometry 2". In this case, for source 1 (78 degrees azimuth) and source 2 (94 degrees azimuth), the optimal configuration has better performance, while for source 3 (114 degrees azimuth), the constrained random configuration has slightly better performance than optimal configuration. In case of "Penrose Geometry 1" (as evident from Fig. 19), the performance of uniform sampling configuration is slightly better than the rest of the configurations. But the difference is not very significant, so we cannot make any strong conclusions about the results of "Penrose Geometry 1".

8. Conclusions

Three sets of aperiodic geometries have been analyzed in this paper. The array geometries were formed based on two types of aperiodic tiling namely Danzer tiling and Penrose tiling. The main motivation behind using these geometries has been to exploit the aperiodic structure of these geometries, as the aperiodic nature of these geometries make the array geometry sparse, which makes it very useful when using compressive sensing based algorithms for DOA estimation of broadband sources. The aperiodic geometry is well suited to the broadband algorithms (in classic non-CS scenario), as this geometry, by virtue of aperiodicity, avoid grating lobes problem, which create ambiguity in DOA estimation for broadband sources. We have seen that using an MMV Compressive Sensing algorithm (SOMP) and using aperiodic geometry based on Danzer tiling we can achieve better performance in terms of MSE than using the uniformly sampled arrays, when the aperture is kept constant. The uniformly sampled arrays use more elements than the aperiodic arrays based on Danzer tiling and Penrose tiling. The aperiodic arrays are inherently sparse which offer advantage in terms of number of sensors used to build an array for a fixed aperture. The optimization formulation is valid for other aperiodic geometries such as fractal geometries. In a nutshell, any geometry that can be represented in $\boldsymbol{p}_u = \boldsymbol{T}_u \boldsymbol{p}$ form, where $\boldsymbol{p}$ contains initial set of points and $\boldsymbol{T}_u$ is a transformation matrix, can be a potential candidate for the optimization scheme developed in this paper.

References

[1] S.Z. Asghar, B.P. Ng, Aperiodic geometry design for DOA estimation using compressive sensing, Intern. Confer. Sampl. Theory Appl. (SampTA), IEEE (2015).
[2] R. Penrose, The role of aesthetics in pure and applied mathematical research, Bullet. Inst. Math. Appl. 10 (2) (1974) 266–271.
[3] H.L.V. Trees, Optimum array processing: Part IV of detection, estimation, and modulation theory, John Wiley & Sons, Inc., 2002.
[4] E. Cand'es, J. Romberg, T. Tao, Robust uncertainty principles: exact signal reconstruction from highly incomplete frequency information, IEEE Trans. Inform. Theory 52 (2) (2006) 489–509.
[5] E. Cand'es, T. Tao, Near optimal signal recovery from random projections: universal encoding strategies? IEEE Trans. Inform. Theory 52 (12) (2006) 5406–5425.
[6] D. Donoho, Compressed sensing, IEEE Trans. Inform. Theory 52 (4) (2006).
[7] E. Cand'es, J. Romberg, T. Tao, Stable signal recovery from incomplete and inaccurate measurements, Comm. Pure Appl. Math. 59 (8) (2006) 1207–1223.
[8] E.J. Candes, M.B. Wakin, An introduction to compressive sampling, IEEE Signal Process. Mag. 25 (2) (2008) 21–30.
[9] D.L. Donoho, M. Elad, V. Temlyakov, Stable recovery of sparse overcomplete representation in the presence of noise, IEEE Trans. Inf. Theory 52 (1) (2006) 6–18.
[10] J.A. Tropp, Greed is good:algorithmic results for sparse approximation, IEEE Trans. Inform. Theory 50 (2004) 2231–2242.
[11] J.A. Tropp, A.C. Gilbert, M.J. Strauss, Algorithms for simultaneous sparse approximation. part i: greedy pursuit, Signal Processing 86 (3) (2006) 572–588.
[12] J. Chen, X. Huo, Theoretical results on sparse representations of multiple-measurement vectors, IEEE Trans. Signal Process. 54 (12) (2006) 4634–4643.
[13] T.G. Spence, D.H. Werner, Design of broadband planar arrays based on the optimization of aperiodic tilings, IEEE Trans. Antennas Propag. 56 (1) (2008) 76–86.
[14] K.P. Nischke, L. Danzer, A construction of inflation rules based on n-fold symmetry, Discrete & Computational Geometry 15 (2) (1996) 221–236.
[15] E. Cand'es, J. Romberg, Sparsity and incoherence in compressive sampling, Inverse Prob. 23 (3) (2007).
[16] M.A. Herman, T. Strohmer, High-resolution radar via compressed sensing, IEEE Trans. Signal Process. 57 (6) (2009) 2275–2284.
[17] J.H.G. Ender, On compressive sensing applied to radar, Signal Process. 90 (2010) 1402–1414.
[18] P.J. Steinhart, Quasicrystals: a brief history of the impossible, Rendiconti Lincei 24 (1) (2013) 85–91. Supplement
[19] D.H. Werner, S. Ganguly, An overview of fractal antenna engineering research, IEEE Antennas Propag. Mag. 45 (1) (2003) 38–57.
[20] R.O. Schmidt, Multiple emitter location and signal parameter estimation, IEEE Trans. Antennas Propag. 34 (3) (1986) 276–280.
[21] W.K. Ma, T.H. Hsieh, C.Y. Chi, DOA Estimation of quasi-stationary signals with less sensors than sources and unknown spatial noise covariance: a khatri-rao subspace approach, IEEE Trans. Antennas Propag. 58 (4) (2010) 2168–2180.
[22] P. Pal, P.P. Vaidyanathan, Nested arrays: a novel approach to array processing with enhanced degrees of freedom, IEEE Trans. Signal Process. 58 (8) (2010) 4167–4181.
[23] S. Qin, Y.D. Zhang, M.G. Amin, Generalized co-prime array configurations for direction-of-arrival estimation, IEEE Trans. Signal Process. 63 (6) (2015) 1377–1390.
[24] D.H. Werner, R.L. Haupt, P.L. Werner, Fractal antenna engineering: the theory and design of fractal antenna arrays, IEEE Antennas Propag. Mag. 41 (5) (1999) 37–59.